Structural Optimization of non-Newtonian Microfluidics

Jensen, Kristian Ejlebjærg; Okkels, Fridolin

Published in:
9. World Congress on Structural and Multidisciplinary Optimization

Publication date:
2011

9th World Congress on Structural and Multidisciplinary Optimization
June 13 -17, 2011, Shizuoka, Japan

Structural Optimization of non-Newtonian Microfluidics

Kristian E. Jensen[1], **Fridolin Okkels**[2]

[1] Technical University of Denmark, Copenhagen, Denmark, kristian.jensen@nanotech.dtu.dk
[2] Technical University of Denmark, Copenhagen, Denmark, fridolin.okkels@nanotech.dtu.dk

1. Abstract
We present results for topology optimization of a non-Newtonian rectifier described with a differential constitutive model. The results are novel in the sense that a differential constitutive model has not been combined with topology optimization previously. We find that it is necessary to apply a filter on the design variables based on a Helmholtz-type differential equation and we try to vary the filter length throughout the optimization in order to ensure compatibility with a convex interpolation between the inverse permeability and the design variables, which is popular within topology optimization of fluids. We test the method on a microfluidic rectifier and find solutions topologically different from experimentally realized designs.
2. Keywords: non-Newtonian; rectifier; Helmholtz density filter; log conformation

3. Introduction
Topology optimization for fluids started out with power minimization in Stokes flow [1], but was later extended to the Navier-Stokes equation and it was in this context, that a generalized high-level implementation for non-linear problems was presented [2].
Mesh dependent solutions are common within the field of structural optimization and a variety of filtering techniques exist to address this, but similar issues are usually not observed in fluidic optimization, because the smallest length scale in the optimal structure is finite. Rather than filtering the design variables or the sensitivities between iterations, one can use an implicit approach in the form of a Helmholtz-type differential equation [3].
Integration of a passive fluid rectifier in a micropump has been demonstrated [4], but most passive rectifiers rely on inertial effects for their working mechanism, so scaling these devices down, will result in vanishing inertial effects and thus also degraded performance. Non-Newtonian rectifiers, which promise size independent performance, have been demonstrated [5] and it is has also been shown that the performance of these devices can be improved by changing the geometry [6].
The performance of non-Newtonian rectifiers is intrinsically related to the fluid memory of past events and therefore it is necessary to apply a differential constitutive model in order to describe a non-Newtonian rectifier. The combination of differential constitutive models with the finite element method has received considerable attention in the scientific community over the past decades. In particular attention has focused around the issue of numerical break down, when the magnitudes of Newtonian and non-Newtonian effects become comparable.

4. Governing Equations
For a Newtonian fluid the stress not due to pressure is simply proportional to the local instantaneous deformation rate. In contrast to this are non-Newtonian fluids where the fluid stress depends on the upstream deformation of the fluid.

4.1 Introduction to Differential Constitutive Models
The first differential constitutive model for a non-Newtonian fluid was proposed by Maxwell, when he suggested that the stress, τ, in a fluid with both viscosity and elasticity was governed by an equation of the form

$$\tau + \lambda \frac{d}{dt}\tau = \eta\dot{\gamma},$$

where λ is a relaxation time for the fluid, η is the viscosity and $\dot{\gamma}$ is the rate of deformation. For changes in stress occurring over a time scale much larger than the relaxation time, the stress reduces to that of a Newtonian fluid. On the other hand changes with a time scale much smaller than the relaxation time will induce a stress, which is proportional and opposite the rate of change.
The model is valid for arbitrary deformations in one dimension, but in its tensor form the model is only valid for small deformations. For large deformations it turns that one has to add geometrical non-linearity to the time derivative in order for the model properties to be invariant with respect to rotation of the coordinate system. The upper convected time derivative is by far the most popular in this context and substituting this for the time derivative in the Maxwell model yields the upper Convected Maxwell Model (UCM):

$$\underline{\underline{\tau}} + \lambda \overset{\nabla}{\underline{\underline{\tau}}} = \eta_p \left[\underline{\underline{\dot{\gamma}}} + \underline{\underline{\dot{\gamma}}}^T\right], \qquad \overset{\nabla}{\underline{\underline{\tau}}} = \frac{D\underline{\underline{\tau}}}{Dt} - \left(\underline{\underline{\tau}} \cdot \underline{\underline{\dot{\gamma}}} + \underline{\underline{\dot{\gamma}}}^T \cdot \underline{\underline{\tau}}\right), \tag{1}$$

where $\underline{\underline{\dot{\gamma}}} = \nabla \underline{v}$ is the deformation tensor, $\overset{\nabla}{\tau}$ is the upper convected derivative and $\frac{D\underline{\underline{\tau}}}{Dt} = \frac{\partial \underline{\underline{\tau}}}{\partial t} + (\underline{v} \cdot \nabla)\underline{\underline{\tau}}$ is the material derivative . In the case of a polymer solution, it is popular to split the stress into a Newtonian and non-Newtonian contribution such that the total fluid stress is equal to

$$\underline{\underline{\tau}} = \eta_s \left[\underline{\underline{\dot{\gamma}}} + \underline{\underline{\dot{\gamma}}}^T\right] + \underline{\underline{\tau}}_p$$

The Oldroyd-B model makes use of such a stress splitting and uses the UCM given in equation (1) as constitutive equation for the polymer stress, τ_p. Most often the flow can be considered incompressible with vanishing inertial effects such the velocity field is divergence free and the Stokes equation with a polymer stress contribution applies.

$$\underline{0} = \nabla \cdot \left(-\underline{\underline{I}}p + \eta_s \left[\underline{\underline{\dot{\gamma}}} + \underline{\underline{\dot{\gamma}}}^T\right] + \underline{\underline{\tau}}_p\right) - \alpha \underline{v}$$

$$0 = \nabla \cdot \underline{v}$$

As usual within the field of topology optimization in fluids we have added a Darcy damping term, $-\alpha \underline{v}$, which serves to impose negligible velocity (and velocity gradients) in solid regions. Due to the fact that the polymeric stress in differential constitutive models is generated by upstream fluid deformation, we believe that this density description of solid and fluid regions is applicable for these models as well.

The Oldroyd-B model is a reference within differential constitutive equations and it can be derived from the starting point of an elastic dumbbell model as sketched in figure 1. The end-to-end vector, $\underline{a}$, describes the polymer orientation and elongation, but rather than using this directly it is the statistical average of the outer product between the end-to-end vector and itself that is used in differential constitutive models. Furthermore this tensor is normalized by the equilibrium length of the end-to-end vector, a_{eq}.

$$\underline{\underline{A}} = \frac{\langle \underline{a} \otimes \underline{a} \rangle}{a_{eq}^2}$$

Many models can be written in a compact form using a differential constitutive equation for the conformation tensor, $\underline{\underline{A}}$, in which case the polymer stress is related to the conformation tensor by an algebraic equation. The average squared extension of the dumbbell can be recovered as the trace of the conformation tensor.

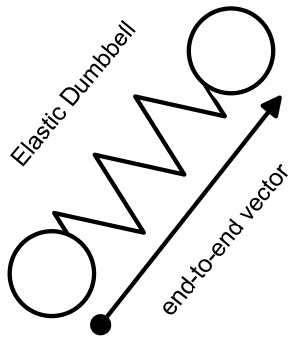

Figure 1: In the Elastic Dumbbell model two point masses are connected by a spring.

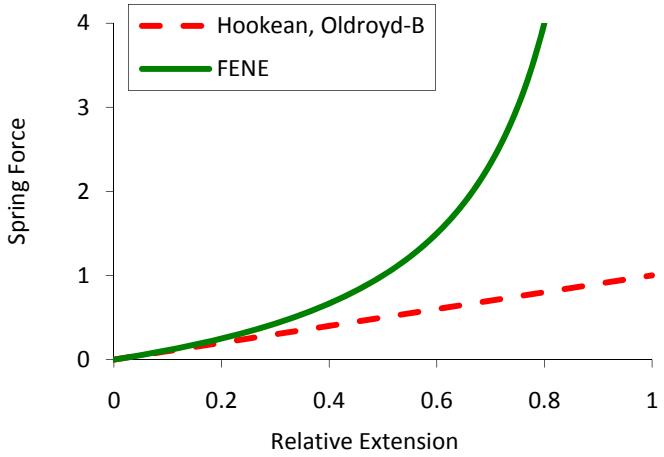

Figure 2: The spring force in the elastic dumbbell model can be Hookean or approach infinite for a certain extension in the case of Finite Extensible (FENE) bead-spring models.

The Oldroyd-B model can be derived as an approximation to an elastic dumbbell assuming a Hookean spring force, but this assumption leads to unlimited extension and other unphysical properties. The dumbbell extension can be restricted by letting the spring force diverge, when the extension reaches a certain value called the extension ability parameter, L, as illustrated in figure 2.

$$F_{\text{spring}} = \frac{k_0}{1 - \text{Tr}(\underline{\underline{A}})/L^2} \text{Tr}(\underline{\underline{A}})$$

Models that are based on such a spring force are called Finite Extensible bead-spring models (FENE).

4.2 Model

Models can be characterized by their properties in simple flows similar to what can be realized experimentally. One example of this is a shear flow, where the rate of deformation tensor is zero except for a single off diagonal term. The ratio between the shear stress and shear rate, in such a flow, is called the shear viscosity.

The experimentally realized rectifiers [5, 6] have been tested with fluids that show a constant shear viscosity and

we therefore choose the finitely extensible bead-spring chain model by Chilcott and Rallison (FENE-CR) [9] as it has this property. Furthermore it has been shown that the transition to time dependent flow can be delayed by decreasing the extension ability parameter in the case of a modified version of the FENE-CR model [10], and the first results with the log-conformation method were in fact produced with the FENE-CR model [11]. In terms of the conformation tensor, $\underline{\underline{A}}$, the FENE-CR equation can be written as

$$\lambda \overset{\nabla}{\underline{\underline{A}}} = -f(\underline{\underline{A}})(\underline{\underline{A}} - \underline{\underline{I}}) \tag{2}$$

$$f\left(\underline{\underline{A}}\right) = \frac{1}{1-\mathrm{Tr}(\underline{\underline{A}})/L^2} \tag{3}$$

$$\underline{\underline{\tau}}_p = \frac{\eta_p f\left(\underline{\underline{A}}\right)}{\lambda}(\underline{\underline{A}} - \underline{\underline{I}}) \tag{4}$$

We introduce dimensionless variables using a characteristic pressure rather than a characteristic velocity.

$$\underline{x} = L\tilde{\underline{x}}, \quad \alpha = \alpha_{\mathrm{char}}\tilde{\alpha}, \quad \underline{v} = \frac{p_{char}L}{\eta_s+\eta_p}\tilde{\underline{v}}, \quad \underline{\underline{\tau}} = p_{\mathrm{char}}\tilde{\underline{\underline{\tau}}}$$

The resulting equations are listed in section 5.1 equations (8-10). The characteristic dimensionless numbers of the system are

$$\mathrm{Da} = \frac{\eta_s+\eta_p}{\alpha_{\mathrm{char}}L^2}, \quad \beta = \frac{\eta_s}{\eta_s+\eta_p}, \quad \mathrm{We} = \lambda\frac{\Delta p_{char}}{\eta_s+\eta_p}$$

The Darcy number, Da, describes the ratio between the Darcy damping term and the sum of viscous and polymer stress terms. β describes the relative magnitude between solvent and polymer viscosity, while the Weissenberg number, We, describes the ratio between the convective timescale and the polymer relaxation time and thus the magnitude of non-Newtonian effects.

Within topology optimization of fluid systems it is common to use the following convex interpolation between the design variables, θ, and the local damping

$$\mathrm{Da}^{-1}\tilde{\alpha}(\theta) = \mathrm{Da}_{\mathrm{min}}^{-1} + (\mathrm{Da}_{\mathrm{max}}^{-1} - \mathrm{Da}_{\mathrm{min}}^{-1})\theta\frac{(1+q)}{\theta+q} \tag{5}$$

The optimization is started with a small value of q, but once converged q is increased and the process is repeated until the interpolation becomes practically linear at $q = 1$.

4.3 Filtering Scheme

We find that is necessary to apply a filtering scheme in order to get meaningful designs with a characteristic length scale larger than the mesh. We choose to impose a minimum length scale, L_{dif}, on the design field, θ, using a Helmholtz type differential equation.

$$L_{\mathrm{dif}}^2\nabla^2\tilde{\theta} = \tilde{\theta} - \theta$$

The filtered design variable, $\tilde{\theta}$, is then substituted for the design variable in the physical problem and in this way the filtering schemes is an integrated part of the sensitivity analysis.

The combination of the interpolation in equation (5) and filtering scheme however gives rise to complications, when the q value is increased. We can study this using a 1D example with a Heaviside step function for the design field, θ, such that the filtered design becomes

$$\tilde{\theta}(x, L_{\mathrm{dif}}) = \begin{cases} \frac{1}{2}e^{x/L_{\mathrm{dif}}} & , x < 0 \\ 1 - \frac{1}{2}e^{-x/L_{\mathrm{dif}}}, & x \geq 0 \end{cases}$$

Plugging this expression into equation (5) enables us to draw curves for the inverse permeability for different values of q as show in figure 3. If we define the effective position of the wall by a critical value of the Darcy number, this effective position changes with q, but we can make the curves intersect by solving

$$\alpha\left(\tilde{\theta}(L_{\mathrm{dif}}^*, L_{\mathrm{dif}}^*, q^*\right) = \alpha\left(\tilde{\theta}(L_{\mathrm{dif}}^*, L_{\mathrm{dif}}), q\right)$$

for L_{dif}, which corresponds to fixing the curve with L_{dif}^* and q^* while changing L_{dif} for the other curves according to

$$\frac{L_{\mathrm{dif}}}{L_{\mathrm{dif}}^*} = \left(1 + \log\left[\frac{q(2(e+q^*)-1)+q^*}{2q^*(q+1)e}\right]\right)^{-1}, \tag{5}$$

Such that they intersect at $x = L_{\mathrm{dif}}^*$ as shown in figure 4, where the curve with the smallest q has been fixed. The downside to this approach is that the filter length quickly becomes smaller than the mesh size effectively disabling the filter.

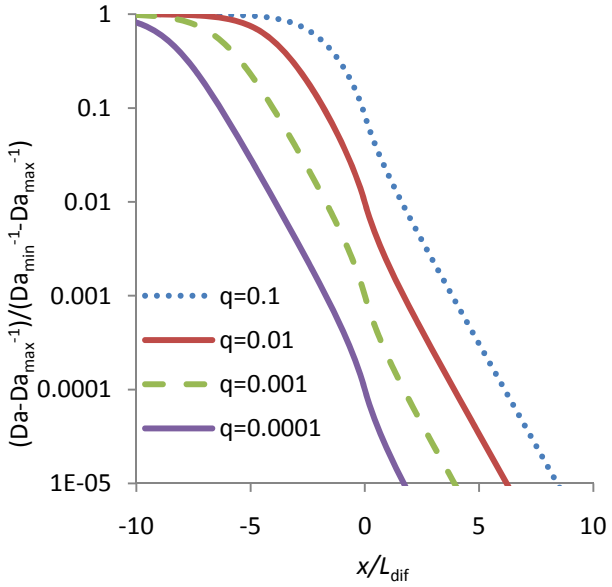

Figure 3: The inverse permeability is plotted for different values of q in the case of a Heaviside step function design variable. The same filter length is used for all q values.

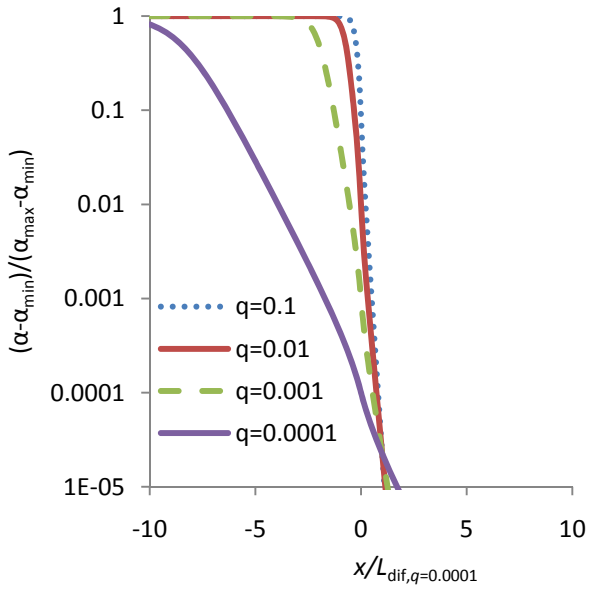

Figure 4: The inverse permeability is plotted for different values of q in the case of a Heaviside step function design variable. The filter length is varied to make the curves intersect.

4.4 Numerical Implementation

The weak formulation of differential constitutive models is a little peculiar in the sense that the rate of deformation tensor is discontinuous, when a second order polynomial basis is used for the velocity vector. Therefore it has shown to be numerically advantageous to introduce a new variable, $\underline{\underline{G}}$, as a continuous approximation to the rate of deformation tensor, but this is not only substituted for the rate of deformation tensor in the constitutive equation, but also incorporated into the Stokes equation via the substitution of $(\underline{\underline{\dot{\gamma}}} - \underline{\underline{G}})/\eta_s + \underline{\underline{G}}$ for the deformation tensor as shown in equation (8). This formulation of the Stokes equation is called the Discreete Elastic Viscous Stress Splitting (DEVSS) and corresponds to adding $\eta_p(\underline{\underline{\dot{\gamma}}} - \underline{\underline{G}})$ as a zero[14].

In the past decades the scientific community has put significant effort into solving what has been known as the High Weissenberg Number Problem (HWNP). The problem relates to the breakdown of numerical finite element codes, when the magnitudes of Newtonian and non-Newtonian effects become comparable. A significant contribution to the solution of this issue was made, when it was shown that the origin of the problem is due to incompatibility between exponential stress growth and the polynomial basis typical of the finite element method [7]. The solution is to write an equation for the evolution of the logarithm of the conformation tensor and solve for this new variable – similar to taking the logarithm of the turbulence variables [8]. The equation for the logarithm of conformation tensor is however still hyperbolic, so it requires stabilization and for this purpose we choose streamline upwind Petrov Gallerkin (SUPG) stabilization. The scheme boils down to replacing the test function A^{test} with $A^{test} + h\underline{v} \cdot \nabla A^{test}$, where $\underline{v}$ is the velocity vector and h is a local characteristic length for the mesh. An overview of the equations in the log conformation form is given in the appendix together with the weak formulation. We apply COMSOL, a high level finite element package, for solving both the physical problem as well as the adjoint problem associated with the sensitivity analysis [2]. Finally we use the Method of Moving Asymptotes (MMA) to update the design variables [12]. The fact that we are able to plug the expressions given in the appendix into this toolbox and get the results of section 5.3 is a testament to the flexibility of topology optimization as a numerical method.

We use linear continuous polynomials for the pressure, the polymer stress and the continuous approximation to the rate of deformation tensor, $\underline{\underline{G}}$. For the velocity vector and the filtered design variable, $\tilde{\theta}$, we use quadratic continuous polynomials, while discontinuous constants describe the design variables, θ. Excluding the design variable there is 12.5 degrees of freedom per interior element.

A good approximate steady solution is determined by time integration, and this approximate solution is used as a starting guess for the iterative solution of the static problem.

We consider the optimization converged at iteration i, when the running averages over the last N iterations of both

the objective function step and infinite norm of the design variable step are below 10^{-5} and 0.1 respectively:
$\frac{1}{N}\sum_{j=i+1-N}^{j=i}\Delta\phi_j = \frac{1}{N}\sum_{i+1-N}^{i}|\phi_j - \phi_{j-1}| < 10^{-5}$ and $\frac{1}{N}\sum_{j=i+1-N}^{j=i}\Delta\theta_j = \frac{1}{N}\sum_{i+1-N}^{i}||\underline{\theta}_j - \underline{\theta}_{j-1}||_\infty < 0.1$
We do not only change the value of L_{dif}, when changing q, but also update the design variables according to

$$\alpha(\theta_{\text{old}}, q_{\text{old}}) = \alpha(\theta_{\text{new}}, q_{\text{new}}) \Rightarrow \theta_{new} = \frac{q_{\text{new}}\theta_{\text{old}}(1+q_{\text{old}})}{q_{\text{old}}+q_{\text{new}}\theta_{\text{old}}+q_{\text{old}}q_{\text{new}}-\theta_{\text{old}}q_{\text{old}}} \tag{6}$$

to preserve α for intermediate values of θ.

5. Results

Experimentally realized non-Newtonian rectifiers produce asymmetric solutions for symmetric designs due to instabilities that arise, when there is a stress along curved streamlines. This behavior is typical at high Weissenberg numbers where the rectification is most efficient, but these solutions are unsteady, so we have to restrict ourselves to optimization at moderate Weissenberg numbers.

5.1 Problem Description

We test the method on the problem of a non-Newtonian rectifier. The problem setup is sketched in figure 5.

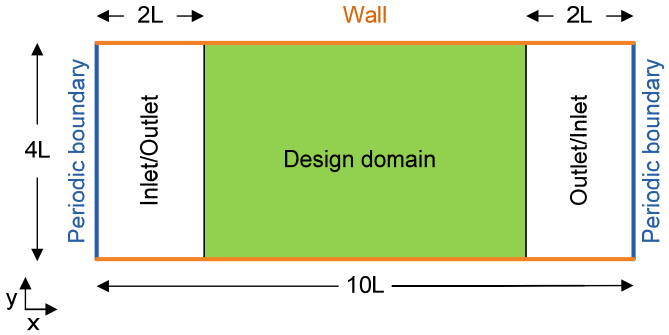

Figure 5: The problem definition for the rectifier is sketched: The flows are pressure driven with a normal stress equal to the pressure on the inlet/outlet boundaries. The conformation tensor and velocity vector are periodic over the inlet/outlet boundaries. At the walls the no slip boundary condition is imposed and to fix the position of the active part of the rectifier, the design domain is restricted to the middle part of the geometry.

We use the flow rate ratio as objective function, and we choose to evaluate the flow rate using the integral of the x component of the velocity vector, v_x, over the domain. We also tried to use the dissipation function, but this improved neither convergence nor the objective function.
Finally we perform the computation of forward flow and related sensitivity analysis in parallel with the computation for the reverse flow. To summarize the optimization problem can be stated as

$$\min_\theta \phi_v = \frac{\int_{\text{domain}} v_{x,\text{reverse}} d\Omega}{\int_{\text{domain}} v_{x,\text{forward}} d\Omega}$$

$$\text{s.t.} \quad \underline{0} = \underline{\tilde{\nabla}} \cdot \left(-\underline{I}\tilde{p} + \left[\underline{\dot{\tilde{\gamma}}} + \underline{\dot{\tilde{\gamma}}}^T - \underline{\tilde{G}} - \underline{\tilde{G}}^T\right] + W\beta\left[\underline{\tilde{G}} + \underline{\tilde{G}}^T\right] + \underline{\tilde{\tau}}_p\right) - \text{Da}_{\min}^{-1}\tilde{\alpha}\underline{\tilde{v}} \tag{7}$$

$$\tilde{\nabla} \cdot \underline{\tilde{v}} = 0, \quad \underline{\tilde{G}} = \underline{\tilde{\nabla}}\underline{\tilde{v}}, \tag{8}$$

$$\underline{\tilde{\tau}}_p = \frac{(1-\beta)f(\underline{A})}{\text{We}}(\underline{A} - \underline{I}), \ \text{We}\overset{\nabla}{\underline{A}} = -f(\underline{A})(\underline{A} - \underline{I}), \ f(\underline{A}) = \frac{1}{1-\text{Tr}(\underline{A})/L^2} \tag{9}$$

$$\text{and} \quad L_{\text{dif}}^2\tilde{\nabla}^2\tilde{\theta} = \tilde{\theta} - \theta. \tag{10}$$

$$\tilde{\alpha}(\tilde{\theta}) = 1 - \tilde{\theta}\frac{(1+q)}{\tilde{\theta}+q}$$

$$0 \le \theta \le 1$$

The weak formulation of the log conformation method is described in the appendix.

5.2 Model Parameters

We choose $\beta = 0.59$, because it is representative for Boger fluids and used widely in benchmarks of numerical algorithms. The transition to time dependent solutions can be delayed to around $\text{We} = 5$ for $L^2 = 100$ [10]. The Weissenberg number is usually defined by a mean velocity and for this reason we choose $\Delta\tilde{p} = 7.17$ as it gives a unit mean velocity for the empty design. We find that we can set $\text{We} = 5$ and still get few unsteady solutions in the optimization. We use an isotropic mesh with a length scale of $h = \frac{L}{5}$ and find stable results for $L_{\text{dif}} = h$. Finally $\text{Da}_{\min} = 10^{-5}$ should be a good compromise between solid walls and numerical convergence while an initial q value of $4 \cdot 10^{-6}$ halves the flow rate compared to the empty design when all design variables are set to 0.5. Once the optimization is converged, we increase q to 10^{-5}, then $3 \cdot 10^{-5}$ and finally 10^{-4}. When increasing q we also

decrease the filter length according to equation (6) and for $q = 10^{-4}$ we get $L_{\text{dif}} \approx h/4$, so increasing q any further effectively disables the filter.

5.3 Results

The optimization results are not discrete as shown in figure 6, but we have no reason to believe that the regions with intermediate design variables are important for the physical working mechanism of the solution. Note that the characteristic length scale of the design is larger than the filter length, so contrary to structural optimization we expect mesh converged solutions, when the filter length scales with the mesh. Figure 7 shows how the optimization converges towards one topology for the initial q value and another for the next. Furthermore the optimization converges towards a symmetric solution, but the first topology and the transition from the first to the second topology is asymmetric. The last frame of figure 7 corresponds to $q = 3 \cdot 10^{-4}$ and it serves to illustrate the small length scales that appear in the absence of filtering. The value of the objective function throughout the optimization is plotted in figure 8, where we see how a very small filter length gives even better objective functions until a certain point where the sensitivity becomes inaccurate or the appearance of unsteady solutions destroys the algorithm convergence.

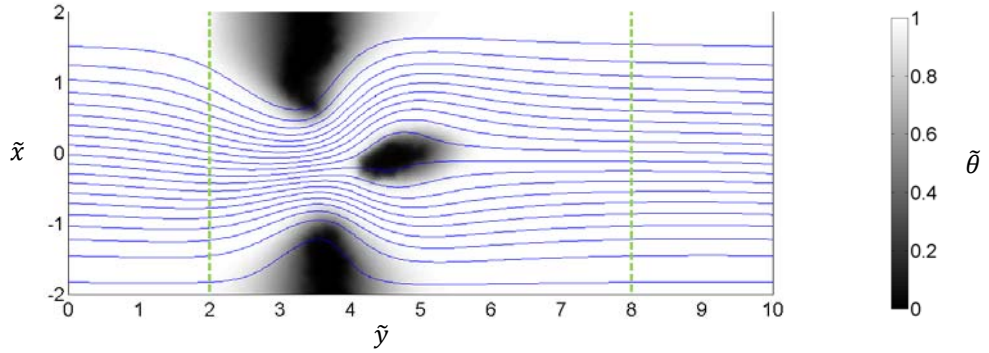

Figure 6: The filtered design variable and streamlines are shown for a converged solution ($q = 10^{-4}$) corresponding to iteration 586 in figure 7. The dashed green lines indicate the position of the design region.

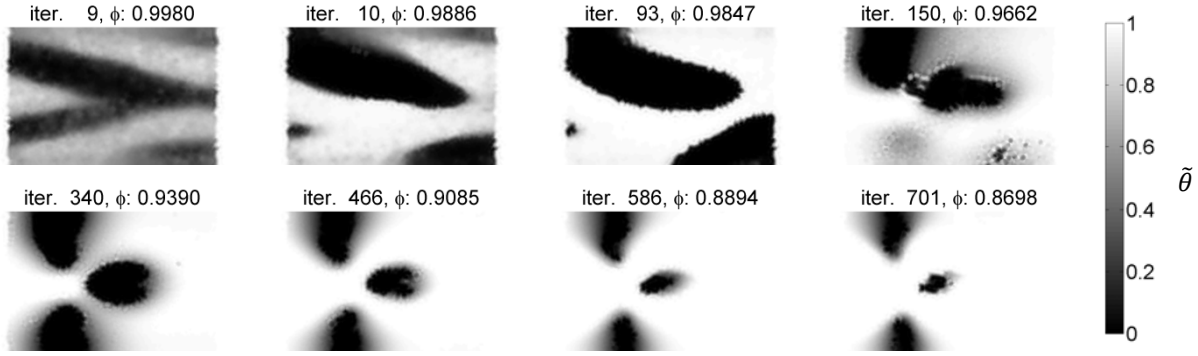

Figure 7: The filtered design variables are shown at representative iterations throughout an optimization. The solution is converged at iterations 93, 340, 466, 586 and 701, so it is after these iterations that q is increased. The filter length starts out at the mesh size, $L_{\text{dif}} = h$, but is reduced to $L_{\text{dif}} = 0.55h$ after iteration 93, which causes a change in topology to a "contraction obstacle"-design.

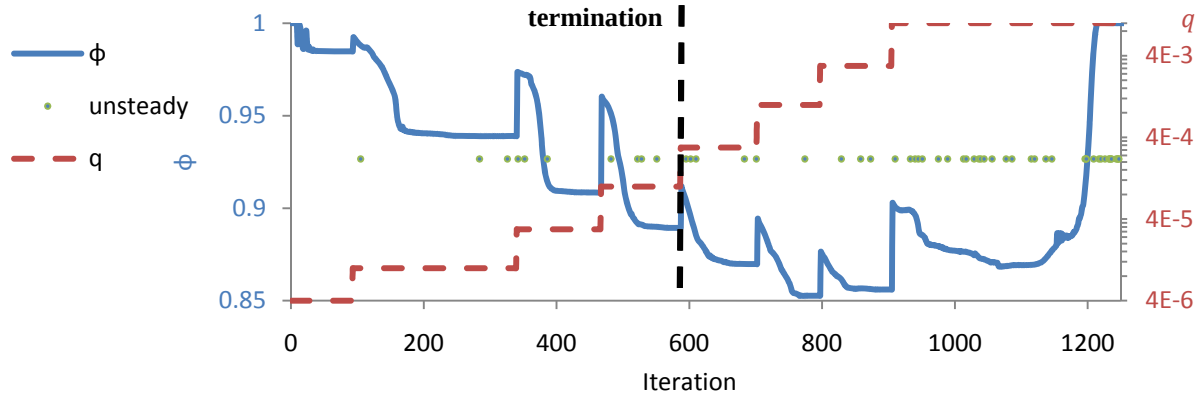

Figure 8: The objective function is plotted throughout an optimization. Green dots indicate that no steady solution could be found. Comparison with figure 7 reveals that the first plateau in the objective function corresponds to a different topology than the other plateaus. The dashed vertical line marks the usual point of termination.

The physical working mechanism of the "contraction obstacle" design is best illustrated in terms of the dumbbell extension shown in figure 9: A region of elongated dumbbells appears in the obstacle wake and for the reverse flow this wake is squeezed by the contraction, which gives rise to an enlarged hydraulic resistance.
The mean velocity at the inlet is around 0.25, but the contraction width can be estimated at $2L$, so the effective Weissenberg number of this design is approximately 2.5.

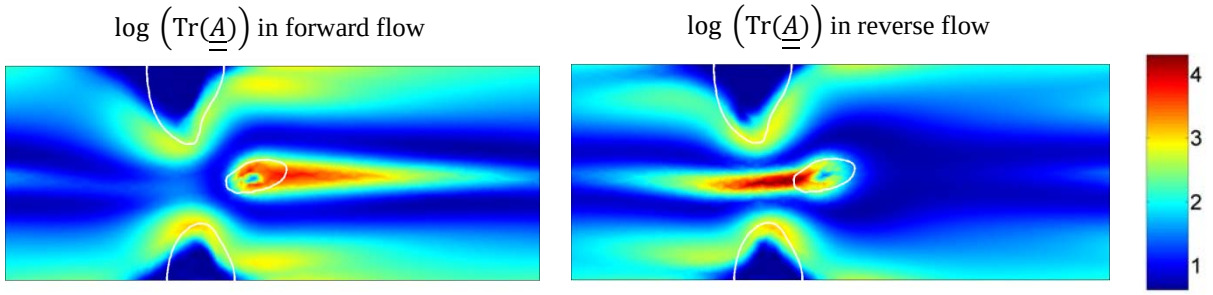

Figure 9: The logarithm of the squared polymer extension is plotted for both flow directions together with the $\tilde{\theta} = \frac{1}{2}$ contour in white. Note that the maximum possible value is restricted to $\log(L^2) \approx 4.6$, so the dumbbells in the obstacle wake are far outside the Hookean regime (see figure 2).

Figure 10 shows an optimization with constant filter length, $L_{\text{dif}} = h/2$. The design is not symmetric, but the working mechanism is the same. The objective function improves as q is increased and it is slightly better at iteration 159 than the optimization with variable filter length at iteration 340 (in figure 7), but otherwise higher such that the design with the smaller filter length has the best objective function for any given q. We expect smaller structures for a constant filter length, because the effective wall position changes (c.f. figure 3), but this is not clearly observed.

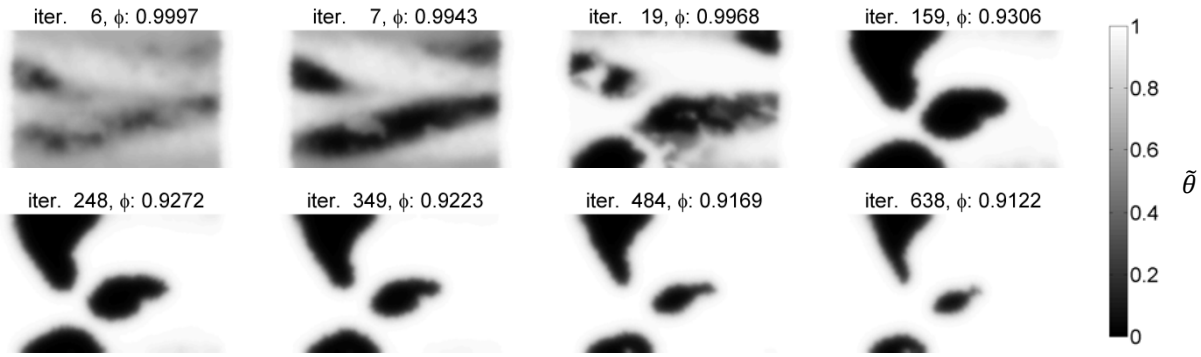

Figure 10: The filtered design variables are shown at representative iterations throughout an optimization with a constant filter length, $L_{\text{dif}} = h/2$. The value of q is increased after the last five frames.

Performing an optimization with a symmetric problem description can result in two obstacles, and this might be due to the fact that the symmetric optimization cannot make an asymmetric transition as the one illustrated in figure 7 rather it follows the route illustrated in figure 11.

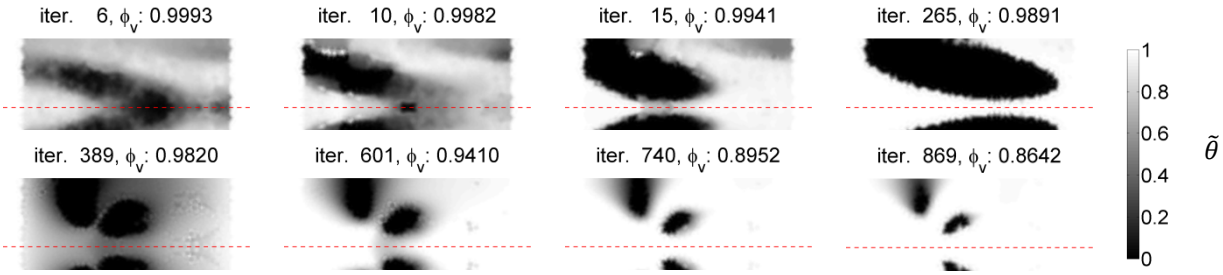

Figure 11: The filtered design variables are shown at representative iterations throughout a symmetric optimization. Note the change of topology from iteration 265 to 389. q is increased at the last five frames.

6. Conclusion

We have presented result for topology optimization of a non-Newtonian rectifier modeled with a FENE-CR fluid using the log conformation method and a Helmholtz type differential equation filter on the design variables. We find topologies different from experimentally realized designs.

7. Acknowledgements

7. References

[1] Borrvall, T., Petersson, J., Topology optimization of fluids in Stokes flow, *International journal for numerical methods in fluids* 41 (1), 77-107, 2003.

[2] Olesen, L., Okkels, F., Bruus, H., A high-level programming-language implementation of topology optimization applied to steady-state Navier-Stokes flow, *International Journal for Numerical Methods in Engineering* 65 (7), 975-1001, 2006.

[3] Lazarov, B., Sigmund, O., Filters in topology optimization based on Helmholtz-type differential equation, *International Journal for Numerical Methods in Engineering*, 2010.

[4] Stemme, E., Stemme, G., A valveless diffuser/nozzle-based fluid pump, *Sensors and Actuators A: physical* 39 (2), 159-167, 1993.

[5] Groisman, A., Quake, S., A microfluidic rectifier: Anisotropic flow resistance at low Reynolds numbers, *Physical review letters* 92 (9), 94501, 2004.

[6] Sousa, P., Pinho, F., Oliveira, M., Alves, M., Efficient microfluidic rectifiers for viscoelastic fluid flow, *Journal of Non-Newtonian Fluid Mechanics* 165, 652-671, 2010.

[7] Hulsen, M., Fattal, R., Kupferman, R., Flow of viscoelastic fluids past a cylinder at high Weissenberg number: stabilized simulations using matrix logarithms, *Journal of Non-Newtonian Fluid Mechanics* 127 (1), 27-39, 2005.

[8] Ilinca, F., Hétu, J., Pelletier, D., A unified finite element algorithm for two-equation models of turbulence, *Computers & Fluids* 27 (3), 291-310, 1998.

[9] Chilcott, M., Rallison, J., Creeping flow of dilute polymer solutions past cylinders and spheres, *Journal of Non-Newtonian Fluid Mechanics* 29, 381-432, 1988.

[10] Oliveira, P., Miranda, A., A numerical study of steady and unsteady viscoelastic flow past bounded cylinders, *Journal of Non-Newtonian Fluid Mechanics* 127 (1), 51-66, 2005.

[11] Fattal, R., Kupferman, R., Constitutive laws for the matrix-logarithm of the conformation tensor, *Journal of Non-Newtonian Fluid Mechanics* 123 (2-3), 281-285, 2004.

[12] Svanberg, K., The method of moving asymptotes – a new method for structural optimization, *International journal for numerical methods in engineering* 24 (2), 359-373, 1987.

[13] Kane, A., Guénette, R., Fortin, A., A comparison of four implementations of the log-conformation formulation for viscoelastic fluid flows, *Journal of Non-Newtonian Fluid Mechanics* 164 (1-3), 45-50, 2009.

[14] Fortin, M., Guenette, R., Pierre, R., Numerical analysis of the modified EVSS method, *Computer methods in applied mechanics and engineering* 143 (1-2), 79-95, 1997.

8. Appendix

The log conformation formulation of equations (2-4) becomes [13]

$$\frac{D\underline{\underline{s}}}{Dt} - \underline{\underline{R}} \cdot \left(\dot{\underline{\underline{\Lambda}}} \cdot \underline{\underline{\Lambda}}^{-1} + \underline{\underline{\widetilde{\Omega}}} \cdot \log(\Lambda) + \log(\Lambda) \cdot \underline{\underline{\widetilde{\Omega}}}^{T}\right) \cdot \underline{\underline{R}}^{T} = \underline{\underline{0}}$$

$$\underline{\underline{\tau}} = \frac{\eta_p f(e^{\underline{\underline{s}}})}{\lambda}\left(e^{\underline{\underline{s}}} - \underline{\underline{I}}\right)$$

$$f(e^{\underline{\underline{s}}}) = \frac{1}{1 - \mathrm{Tr}(e^{\underline{\underline{s}}})/L^2}$$

Here the logarithm of conformation tensor, $\underline{\underline{s}}$, has been introduced together with the rotation tensor, $\underline{\underline{R}}$, holding the normalized eigenvectors of the conformation tensor[1] in the columns. The computation of the eigenvalues and eigenvectors of $\underline{\underline{s}}$ is at the heart of the method.

We introduce a (small) numerical parameter ϵ such that when $|s_{12}| < \epsilon$

$$\underline{\underline{R}} = \underline{\underline{I}}, \qquad |s_{12}| < \epsilon$$

is used (otherwise equation (12)). The conformation tensor can be recovered as

$$\underline{\underline{A}} = e^{\underline{\underline{s}}} = \underline{\underline{R}} \cdot \mathrm{e}^{\underline{\underline{\Sigma}}} \cdot \underline{\underline{R}}^{T}$$

Where, $\mathrm{e}^{\underline{\underline{\Sigma}}}$, is a diagonal matrix with the exponentials of the eigenvalues of $\underline{\underline{s}}$. The trace of the conformation tensor is equal to the sum of its eigenvalues, so for two dimensions we have

$$f(e^{\underline{\underline{s}}}) = \frac{1}{1 - (\lambda_1 + \lambda_2)/L^2}$$

The matrix $\dot{\underline{\underline{\Lambda}}} \cdot \underline{\underline{\Lambda}}^{-1}$ is diagonal and (switching to index notation) it is equal to

$$\left(\dot{\underline{\underline{\Lambda}}} \cdot \underline{\underline{\Lambda}}^{-1}\right)_{ii} = 2\tilde{G}_{ii} - f(e^{\underline{\underline{s}}})\frac{\lambda_i - 1}{\lambda},$$

where λ_i are the eigenvalues[2] of $\underline{\underline{s}}$ and λ is the relaxation time. $\underline{\underline{\tilde{G}}}$ is given by

$$\underline{\underline{\tilde{G}}} = \underline{\underline{R}}^{T} \cdot \underline{\underline{\mathrm{G}}} \cdot \underline{\underline{R}}$$

Finally $\underline{\underline{\widetilde{\Omega}}} \cdot \log(\Lambda) + \log(\Lambda) \cdot \underline{\underline{\widetilde{\Omega}}}^{T}$ is symmetric and with zero diagonal entries and off diagonal entries equal to

$$\left(\underline{\underline{\widetilde{\Omega}}} \cdot \log(\Lambda) + \log(\Lambda) \cdot \underline{\underline{\widetilde{\Omega}}}^{T}\right)_{ij} = \frac{\log(\lambda_i) - \log(\lambda_j)}{\lambda_i - \lambda_j}(\lambda_i \tilde{\tilde{G}}_{ji} + \lambda_j \tilde{G}_{ij})$$

In the limit of equal eigenvalues corresponding to $|\lambda_i - \lambda_j| < \epsilon$, we use

$$\left(\underline{\underline{\widetilde{\Omega}}} \cdot \log(\Lambda) + \log(\Lambda) \cdot \underline{\underline{\widetilde{\Omega}}}^{T}\right)_{ij} = \tilde{\tilde{G}}_{ji} + \tilde{G}_{ij}, \qquad |\lambda_i - \lambda_j| < \epsilon$$

The complete weak form of the equations will written in the following with *x* and *y* subscripts indicating differentiation. Furthermore the velocity vector components are denoted u and v.

Stokes equation

$$\left[p + 2\left((1-\eta_s)G_{11} - u_x\right) - \tau_{11}\right]u_x^{test} + \left[(1-\eta_s)(G_{12}+G_{21}) - \left(u_y + v_x\right) - \tau_{12}\right]u_y^{test} + [\alpha u]u^{test} = 0$$

$$\left[(1-\eta_s)(G_{12}+G_{21}) - \left(u_y + v_x\right) - \tau_{12}\right]v_x^{test} + \left[p + 2\left((1-\eta_s)G_{22} - v_y\right) - \tau_{22}\right]v_y^{test} + [\alpha v]v^{test} = 0$$

$$\left[u_x + v_y\right]p^{test} = 0,$$

The continuous approximation of the deformation tensor

$$[u_x - G_{11}]G_{11}^{test} = 0, \quad \left[u_y - G_{12}\right]G_{12}^{test} = 0, \quad [v_x - G_{21}]G_{21}^{test} = 0, \quad \left[v_y - G_{22}\right]G_{22}^{test} = 0$$

The polymer stress tensor

$$\left[T_{11} - \frac{f\eta_p}{\lambda}(A_{11} - 1)\right]\tau_{11}^{test} = 0, \quad \left[T_{12} - \frac{f\eta_p}{\lambda}A_{12}\right]\tau_{12}^{test} = 0, \quad \left[T_{22} - \frac{f\eta_p}{\lambda}(A_{22} - 1)\right]\tau_{22}^{test} = 0,$$

The logarithm of the conformation tensor

$$\left[\frac{\partial s_{11}}{\partial t} + u \cdot s_{11x} + v \cdot s_{11y} - \Pi_{11}\right]\left[s_{11}^{test} + h(u \cdot s_{11x}^{test} + v \cdot s_{11y}^{test})\right] = 0$$

$$\left[\frac{\partial s_{12}}{\partial t} + u \cdot s_{12x} + v \cdot s_{12y} - \Pi_{12}\right]\left[s_{12}^{test} + h(u \cdot s_{12x}^{test} + v \cdot s_{12y}^{test})\right] = 0$$

$$\left[\frac{\partial s_{22}}{\partial t} + u \cdot s_{22x} + v \cdot s_{22y} - \Pi_{22}\right]\left[s_{22}^{test} + h(u \cdot s_{22x}^{test} + v \cdot s_{22y}^{test})\right] = 0$$

where the eigenvalues, λ_1 and λ_2 of the conformation tensor, $\underline{\underline{A}}$, are calculated as

[1] The eigenvectors of the logarithm of the conformation tensor are identical to those of the conformation tensor.

[2] The eigenvalues of the conformation tensor, $\underline{\underline{A}}$, are the exponential of the eigenvalues of $\underline{\underline{s}}$.

$$\lambda_1' = \frac{1}{2}\left(S_{22}+S_{11}-\sqrt{|S_{22}^2+S_{11}^2-2S_{22}S_{11}+4S_{12}^2|}\right),\ \ \lambda_2' = \frac{1}{2}\left(S_{22}+S_{11}+\sqrt{|S_{22}^2+S_{11}^2-2S_{22}S_{11}+4S_{12}^2|}\right),\qquad \lambda_1 = e^{\lambda_1'},\ \ \lambda_2 = e^{\lambda_2'}$$

and the components, v_{1x} and v_{1y}, of the first normalized eigenvector are

$$v_{1x}' = \left[-\frac{S_{12}}{S_{11}-\lambda_1}\right]\cdot\{|S_{12}|<\epsilon\}+\{|S_{12}|\geq\epsilon\},\ v_{1y} = \{|S_{12}|<\epsilon\},\ v_{1x} = \frac{v_{1x}'}{\sqrt{{v_{1x}'}^2+{v_{1y}'}^2}},\ v_{1y} = \frac{v_{1y}'}{\sqrt{{v_{1x}'}^2+{v_{1y}'}^2}}$$

Here we have used a boolean expression to treat the special case ($|S_{12}|<\epsilon$). We can thus write the transformation tensor

$$\underline{\underline{R}} = \begin{bmatrix} v_{1x} & -v_{1y} \\ v_{1y} & v_{1x} \end{bmatrix} \tag{11}$$

We then proceed to calculate the conformation tensor

$$A_{11} = v_{1x}^2 e^{\lambda_1'} + v_{1y}e^{\lambda_2'}, A_{12} = v_{1x}v_{1y}\left(e^{\lambda_1'}-e^{\lambda_2'}\right), A_{22} = v_{1y}^2 e^{\lambda_1'} + v_{1x}e^{\lambda_2'}$$

and $\underline{\underline{\tilde{G}}}$

$$\tilde{G}_{11} = v_{1x}^2G_{11}+v_{1x}v_{1y}(G_{12}+G_{21})+v_{1y}^2G_{22}, \tilde{G}_{12} = v_{1x}v_{1y}(G_{22}-G_{11})+v_{1x}^2G_{21}-v_{1y}^2G_{12}$$
$$\tilde{G}_{21} = v_{1x}v_{1y}(G_{22}-G_{11})-v_{1y}^2G_{21}+v_{1x}^2G_{12}, \tilde{G}_{22} = v_{1y}^2G_{11}-v_{1x}v_{1y}(G_{12}+G_{21})+v_{1x}^2G_{22}$$

Then the diagonal components $\underline{\underline{\dot{\Lambda}}}\cdot\underline{\underline{\Lambda}}^{-1}$ are calculated

$$\Lambda_{11} = 2\tilde{G}_{11}+\frac{f_{11}}{\lambda_1}, \Lambda_{22} = 2\tilde{G}_{22}+\frac{f_{22}}{\lambda_2}, f_{11} = -\frac{1}{1-(\lambda_1+\lambda_2)/L^2}\frac{[\lambda_1-1]}{\lambda}\ f_{22} = -\frac{1}{1-(\lambda_1+\lambda_2)/L^2}\frac{[\lambda_2-1]}{\lambda}$$

Note that the λ without the subscript refers to the polymer relaxation time. We can now proceed to calculate the off diagonal expression for $\underline{\underline{\tilde{\Omega}}}\cdot\log(\Lambda)+\log(\Lambda)\cdot\underline{\underline{\tilde{\Omega}}}^T$

$$\Lambda_{12} = \left[\frac{\log(\lambda_1)-\log(\lambda_2)}{\lambda_1-\lambda_2}\left(\lambda_1\tilde{\tilde{G}}_{12}+\lambda_2\tilde{G}_{21}\right)\right]\{|S_{12}|<\epsilon\}+\left[\tilde{\tilde{G}}_{12}+\tilde{G}_{21}\right]\cdot\{|S_{12}|\geq\epsilon\}$$

Finally we can write the expressions for $\underline{\underline{\Pi}}$

$$\Pi_{11} = v_{1x}^2\Lambda_{11}+v_{1y}^2\Lambda_{22}+v_{1x}v_{1y}\Lambda_{12}$$
$$\Pi_{12} = v_{1x}v_{1y}(\Lambda_{11}-\Lambda_{22})+\left(v_{1x}^2-v_{1y}^2\right)\Lambda_{12}$$
$$\Pi_{22} = v_{1y}^2\Lambda_{11}+v_{1x}^2\Lambda_{22}+v_{1x}v_{1y}\Lambda_{12}$$